



Aeroelastic behaviour of a parameterised circulation-controlled wing

Nora Neuert¹ · Dieter Dinkler¹

Received: 29 January 2018 / Revised: 22 October 2018 / Accepted: 21 November 2018 / Published online: 12 March 2019
© Deutsches Zentrum für Luft- und Raumfahrt e.V. 2019

Abstract

The aeroelastic behaviour of the wing of a short take-off and landing aircraft using the Coandă effect depends on its properties and shape. An existing reduced-order model is parameterised for detailed investigations. On the one hand, varying mass due to tank level and varying overall stiffness is implemented in the reduced-order model. The influence of the mass change on the aeroelastic behaviour is reflected in the stability maps. On the other hand, two-dimensional steady and unsteady aerodynamics of different nose shapes are investigated with detailed computational fluid simulations and included in the reduced-order model. The dependence on the profile shape and the frequency is described. Their influence on the aeroelastic behaviour is reflected by the stability maps as well.

Keywords Aeroelasticity · Circulation control · Parameterisation · Reduced-order model

List of symbols

A_{ref}	Reference wing area	ω	Natural frequency
c_L	Lift coefficient	ω_i	i -th natural frequency
c_M	Pitching moment coefficient	\mathbf{A}_0	Aerodynamic stiffness matrix
c_p	Pressure coefficient	\mathbf{A}_1	Aerodynamic damping matrix
c_μ	Momentum coefficient of the circulation control	\mathbf{K}	Stiffness matrix
f	Frequency	\mathbf{L}	Aerodynamic load vector
g	Net weight	\mathbf{M}	Mass matrix
h	Heave displacement	\mathbf{X}	Modal matrix
l	Chord length	\mathbf{q}	Vector of generalised coordinates
m	Mass	\mathbf{x}	Vector of physical degrees of freedom
\dot{m}_{jet}	Mass flow in the Coandă slot	$\hat{\mathbf{x}}_i$	i -th eigenvector
q	Generalised coordinate	$()_0$	Constant part
q_∞	Dynamic pressure	$()_1$	Referring to the initial configuration
v_∞	Approach velocity	$()_2$	Referring to the altered configuration
v_{jet}	Jet velocity in the Coandă slot	$()_A$	Referring to the discretisation of the aerodynamic model
α	(Effective) angle of attack	$()_{,\text{droop}}$	Referring to droop nose
γ_i	i -th participation factor	$()_S$	Referring to the discretisation of the structural model
δ_{fl}	Flap deflection	$\Delta()$	Deviation of variable
η	Dimensionless chord	$\dot{()}$	Derivative with respect to time
η_k	Parameterised stiffness	$()_{,x}$	Derivative with respect to x
η_m	Parameterised tank level		

✉ Nora Neuert
n.neuert@tu-bs.de

Dieter Dinkler
d.dinkler@tu-bs.de

¹ TU Braunschweig, Institute of Structural Analysis,
Beethovenstr. 51, 38106 Brunswick, Germany

1 Introduction

To cover the continuously rising air traffic, the use of small, existing airports needs to be extended. This comes along with several problems. For one, the small airports are close

to populated areas calling for emission reduction regarding fuel and noise. Furthermore, their runways are shorter than the ones of large airports. To use these short runways, the aircraft design has to be improved significantly.

The Coordinated Research Centre SFB 880 [1] is investigating an aircraft with short take-off and landing capabilities in accordance with the vision *Flightpath 2050* [2]. The wing is, therefore, equipped with various technologies. At the trailing edge flap active circulation control making use of the Coandă effect is employed. The leading edge is equipped with a morphing droop nose to raise the stall angle [3].

The aerodynamic aspect of lift gain in steady-state flow with active circulation control has been investigated extensively [4–8]. The aeroelastic aspect, however, was investigated to a lesser extent [9, 10]. Haas and Chopra [11] detected an additional heave flutter phenomenon occurring only with active circulation control and, therefore, named it *circulation control flutter*. In contrast to the quasi-elliptical profile without a flap examined by Haas and Chopra, a profile with a Coandă flap and two different leading edge shapes are subject of the current research.

A reduced-order model (ROM) is derived from a full-scale three-dimensional finite element wing model and used for detailed studies. The underlying ROM [15] already considers differing aerodynamic forces due to angle of attack α , flap angle δ_{fl} and circulation control, represented by c_{μ} for the clean nose configuration.

Recently, four new parameters have been included in the ROM:

- mass variation η_m
- stiffness variation η_k
- shape of profile
- natural frequency ω

The bending flutter phenomenon due to circulation control is displayed by the results. Variations of the nose shape, mass distribution and exciting frequency are considered and differences identified.

All results of numerical flow simulations presented in this paper are computed with the *DLR TAU* code of the German Aerospace Center [18], an unstructured finite volume code solving the Reynolds-averaged Navier–Stokes equations (RANS). The original Spalart–Allmaras model is used for turbulence modelling [19].

2 High-lift devices

In 1800, Thomas Young described the fundamental phenomenon of the Coandă effect [12]. Surrounding free stream flow is more reluctant to follow a curved surface than a thin jet. Accordingly, a thin jet is blown out

upstream of the plain flaps and aileron to deflect the flow. Hence, the so-called Coandă flap may be deflected up to 80° , causing additional lift [13, 14]. A momentum coefficient, describing the normalised jet momentum on the slot, represents the activated amount of circulation control (cf. [10]). The ratio of introduced jet momentum per time at the jet exit section $\dot{m}_{\text{jet}} v_{\text{jet}}$ is set to proportion to the freestream dynamic pressure q_{∞} and the wing reference area A_{ref} :

$$c_{\mu} = \frac{\dot{m}_{\text{jet}} v_{\text{jet}}}{q_{\infty} A_{\text{ref}}}. \quad (1)$$

Three different flow conditions due to the active circulation control may be observed. Figure 1 shows that a momentum coefficient of $c_{\mu} = 0.027$ leads to a partially adjacent flow on the Coandă flap. Nevertheless, the flow separates before reaching the trailing edge. Thus, this regime is referred to as “boundary layer control”. When the flow is attached over the whole range whilst using little power, the most efficient momentum coefficient is reached. Further increasing the momentum coefficient, e.g. $c_{\mu} = 0.054$, leads to a jet effect and continuous deflection of the streamlines after the trailing edge. In this “supercirculation” regime lift is still enhanced, but the ratio of power input to lift gain declines. To further increase lift gain and to reduce the power required for the high-lift device, the leading edge shape of the wing is modified into a droop nose [3]. The profile shapes are pictured in Fig. 2a.

The impact of the Coandă jet and designed droop nose on the pressure distribution of the wing can be seen in Fig. 2b. The suction peak at the leading edge of the clean nose configuration accounts for its stalling mechanism [3]. This suction peak is significantly reduced and spread over a wider range by the droop nose modification. An additional suction area is induced on the Coandă flap.

Together with the suction area at the leading edge, the Coandă jet provides for the endangered heave flutter.

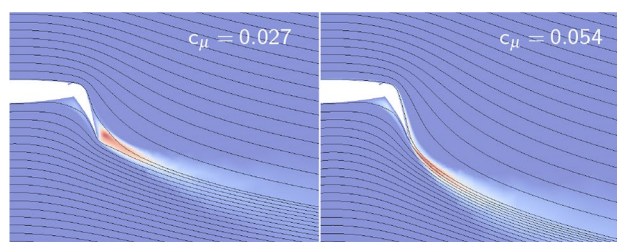


Fig. 1 Flow around the trailing edge with $\delta_{\text{fl}} = 65^\circ$, $\alpha = 0^\circ$ and $v_{\infty} = 51$ m/s with boundary layer control and supercirculation

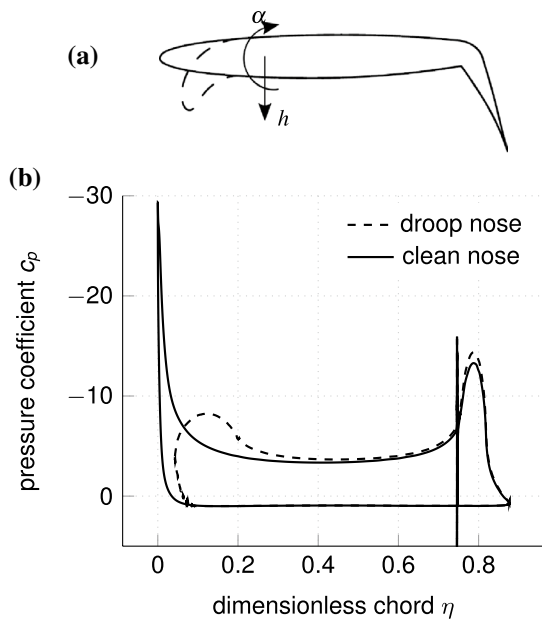


Fig. 2 Comparison of pressure distribution with $\delta_n = 65^\circ$, $\alpha = 0^\circ$, $c_\mu = 0.054$ and $v_\infty = 51$ m/s

3 Reduced-order model

The fundamental setup of the ROM based on the strip theory is described by Krukow and Dinkler [15]. It is adapted from the three-dimensional finite element model described by Sommerwerk et al. [16]. Over the years, different reference configurations are investigated in the Coordinated Research Centre. The following ROM is based on the REF2-2013 configuration presented in Sommerwerk et al. [17], focussing on the wing without the tractor propeller engine. The engine is considered as a mass point, connected to the wing with rigid beam elements.

On the structure side, the former ROM [15] is enhanced by parameters η_m and η_k to allow for changes in mass and stiffness distribution.

3.1 Structure

The wing structure is described by the equation of motion

$$\mathbf{M}_{1S}\ddot{\mathbf{x}}_S + \mathbf{K}_{1S}\mathbf{x}_S = \mathbf{g}_S, \tag{2}$$

with \mathbf{M}_{1S} being the mass and \mathbf{K}_{1S} the stiffness matrix of the initial configuration. \mathbf{x}_S describes the displacement degrees of freedom and \mathbf{g}_S is the structures' net weight. Via the modal approach

$$\mathbf{x}_S = \mathbf{X}\mathbf{q}, \tag{3}$$

with \mathbf{q} being the vector of generalised coordinates and \mathbf{X} the modal matrix, containing the natural modes $\hat{\mathbf{x}}_{1i}$ of the wing, Eq. (2) is decoupled. For each natural mode i results

$$\ddot{q}_i + \omega_{1i}^2 q_i = \gamma_i g. \tag{4}$$

Thus, the structure may be described by selected eigenfrequencies ω_{1i} and participation factors γ_i .

Deviating mass or stiffness distribution influences these properties. Therefore, it is desirable to parameterise the ROM. The mass distribution due to tank level or the structural stiffness due to the flap deflection angle or nose configuration are considered by parameters η_m and η_k .

A second configuration with deviating mass and stiffness matrices

$$(\mathbf{M}_{1S} + \Delta\mathbf{M}_S)\ddot{\mathbf{x}}_S + (\mathbf{K}_{1S} + \Delta\mathbf{K}_S)\mathbf{x}_S = 0, \tag{5}$$

leads to altered eigenvectors $\hat{\mathbf{x}}_{2i}$ and natural frequencies ω_{2i} . To parameterise the structure, the second configuration needs to be described in terms of the initial configuration. This is achieved by describing the displacement degrees of freedom in terms of the eigenvectors of the initial configuration:

$$\mathbf{x}_S = \hat{\mathbf{x}}_{1i} q_i \quad \ddot{\mathbf{x}}_S = \hat{\mathbf{x}}_{1i} \ddot{q}_i. \tag{6}$$

Inserting this approach to Eq. (5) and multiplying it by the transposed eigenvectors yields

$$\hat{\mathbf{x}}_{1i}^T (\mathbf{M}_{1S} + \Delta\mathbf{M}_S) \hat{\mathbf{x}}_{1i} \ddot{q}_i + \hat{\mathbf{x}}_{1i}^T (\mathbf{K}_{1S} + \Delta\mathbf{K}_S) \hat{\mathbf{x}}_{1i} q_i = 0, \tag{7}$$

respectively,

$$(1 + \underbrace{\hat{\mathbf{x}}_{1i}^T \Delta\mathbf{M}_S \hat{\mathbf{x}}_{1i}}_{\eta_m \Delta m_i}) \ddot{q}_i + (\omega_{1i}^2 + \underbrace{\hat{\mathbf{x}}_{1i}^T \Delta\mathbf{K}_S \hat{\mathbf{x}}_{1i}}_{\eta_k \Delta \omega_i^2}) q_i = 0. \tag{8}$$

With an altered generalised mass Δm_i and altered generalised natural frequencies $\Delta \omega_i$, the equation of motion may be described via the initial natural frequencies and two parameters η_m and η_k . The natural frequencies of the second configuration approximately result in

$$\omega_{2i}^2 \approx \frac{\omega_{1i}^2 + \eta_k \Delta \omega_i^2}{1 + \eta_m \Delta m_i}. \tag{9}$$

The altered generalised mass and frequencies are determined with a distinction of cases. First, altering the mass $\eta_m = 1$ and leaving the stiffness unchanged $\eta_k = 0$ leads to

$$\Delta m_i = \frac{\omega_{1i}^2}{\omega_{2i}^2} - 1, \tag{10}$$

whereas altering the stiffness $\eta_k = 1$ and leaving the mass unchanged $\eta_m = 0$ yields

$$\Delta\omega_i^2 = \omega_{2i}^2 - \omega_{1i}^2 \tag{11}$$

Thus, stiffness and tank level in the ROM are provided by the parameters η_k and η_m .

3.2 Structural mode shapes

The first eight structural mode shapes of the droop nose configuration with full tank $\eta_m = 1.3$ and a flap deflection angle of $\delta_{fl} = 65^\circ$ are displayed in Fig. 3. The first mode is the first flap bending mode, followed by another bending mode induced by the engine mass. Modes 3 and 6 are predominantly inplane modes. Since the engine and drag forces are neglected in the aerodynamic model, the corresponding modes are not considered. The second, third and fourth flap bending modes are represented by the modes four, five and eight. While mode five already covers some torsion, mode seven is the first pure torsion mode.

Varying the nose shape and flap deflection angle has little influence on the general mode shapes. Varying the fuel mass, however, primarily influences the natural frequencies and shapes. Figure 4 shows the declining natural frequencies with increasing tank fill levels. The labels correspond to the mode shapes displayed in Fig. 3. It can be seen that modes 5 and 7 become indistinct at a certain tank fill level and trade places for small tank fill levels.

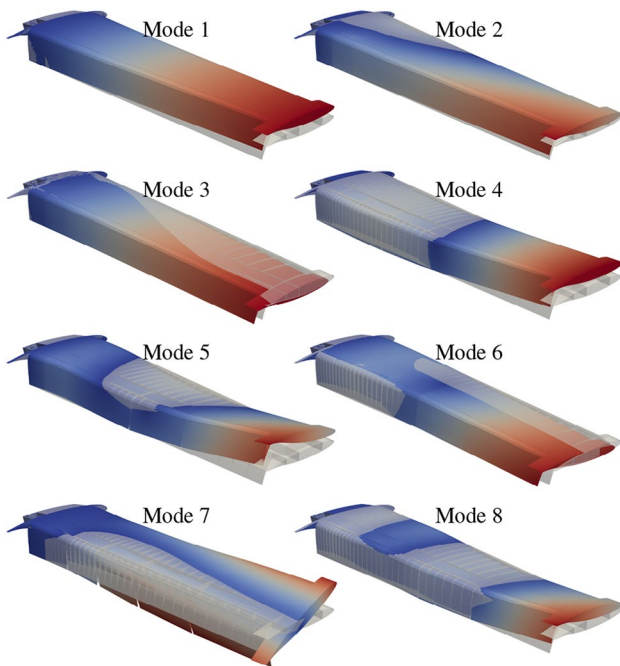


Fig. 3 First eight mode shapes of model with droop nose with full tank, deformation scaled by a factor of five

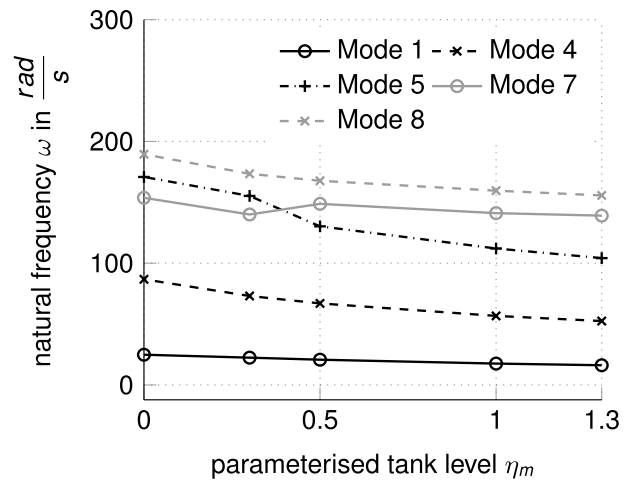


Fig. 4 Natural frequencies over tank level η_m

4 Aerodynamics

For a better understanding of the phenomena, the two-dimensional aerodynamics are investigated in detail. The considered approach velocity for all simulations is about $v_\infty = 51$ m/s.

The steady aerodynamics are extended by lift and moment coefficients for the droop nose configuration and compared to the clean nose configuration.

The unsteady aerodynamics for both nose shapes are investigated for a heave and pitch motion with an impulse procedure [22, 23] to account for frequency dependence.

4.1 Steady aerodynamics

The results for the clean nose are approximated by a mathematical smoothing function, depending on the local angle of attack α , flap deflection angle δ_{fl} and momentum coefficient c_μ given in [20]. The results for the droop nose are approximated by the following smoothing functions, also depending on the local angle of attack α and momentum coefficient c_μ for a flap deflection angle of $\delta_{fl} = 65^\circ$:

$$c_{L,droop} = 3.35 + 33.17 c_\mu + (7.95 - 83.7 c_\mu) \alpha - (27.53 - 632.5 c_\mu) \alpha^2 - (0.318 - 7.58 c_\mu) 10^3 \alpha^3 + (0.12 - 3.37 c_\mu) 10^4 \alpha^4 \tag{12}$$

$$c_{M,droop} = -0.65 - 7.53 c_\mu - (0.39 - 17.7 c_\mu) \alpha + (6.51 - 125.8 c_\mu) \alpha^2 + (0.64 - 14.9 c_\mu) 10^2 \alpha^3 - (2.64 - 68.9 c_\mu) 10^2 \alpha^4. \tag{13}$$

Only lift and pitching moment are considered, described by their dimensionless coefficients

$$\begin{bmatrix} c_L \\ c_M \end{bmatrix} = \begin{bmatrix} c_{L0} \\ c_{M0} \end{bmatrix} + \begin{bmatrix} 0 & c_{L\alpha} \\ 0 & c_{M\alpha} \end{bmatrix} \begin{bmatrix} h \\ \alpha \end{bmatrix} + \frac{1}{v_\infty} \begin{bmatrix} c_{Lh} & l c_{L\dot{\alpha}} \\ c_{Mh} & l c_{M\dot{\alpha}} \end{bmatrix} \begin{bmatrix} \dot{h} \\ \dot{\alpha} \end{bmatrix} \tag{14}$$

with the pitching moment being related to the quarter chord. The aerodynamic mass inertia is ignored and the terms are made dimensionless by the chord length l and the freestream velocity v_∞ .

The lift coefficients of the clean and droop nose for different momentum coefficients c_μ are compared in Fig. 5. While all momentum coefficients relate to the supercirculation regime, an increase in maximum lift $c_{L,max}$ is still observed. For the clean nose configuration, this is accompanied by a decrease in corresponding angle of attack $\alpha_{c_L,max}$ to 1° with a momentum coefficient $c_\mu = 0.054$. Increasing the angle of attack beyond $\alpha_{c_L,max}$ leads to a decrease in lift; however, the flow is not separated. This behaviour is referred to as c_μ - α -stall [11]. An increasing boundary layer thickness leads to less effective circulation control in this regime [7].

Whereas the suction peak at the leading edge of the clean nose (s. Fig. 2) causes large losses of momentum, the droop nose configuration is less sensitive to momentum variation. The thickness of the boundary layer is smaller and remains almost constant with varying momentum coefficients [3]. $\alpha_{c_L,max}$ is shifted by 10° . The maximum lift of the clean nose is reached with the droop nose at 8° with a momentum coefficient of $c_\mu = 0.039$ (s. filled marks Fig. 5). Therefore, the droop nose needs less energy to reach the same lift.

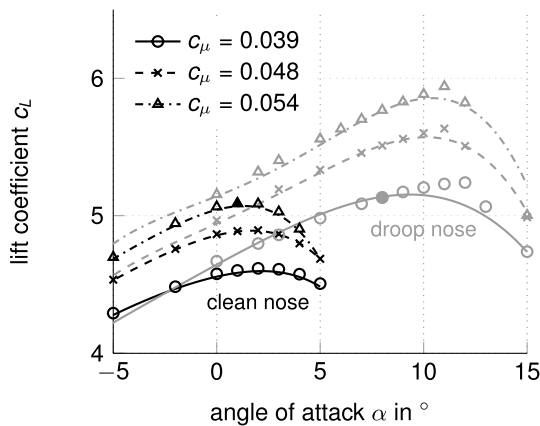


Fig. 5 Lift coefficient for clean nose and droop nose with $\delta_{n_i} = 65^\circ$

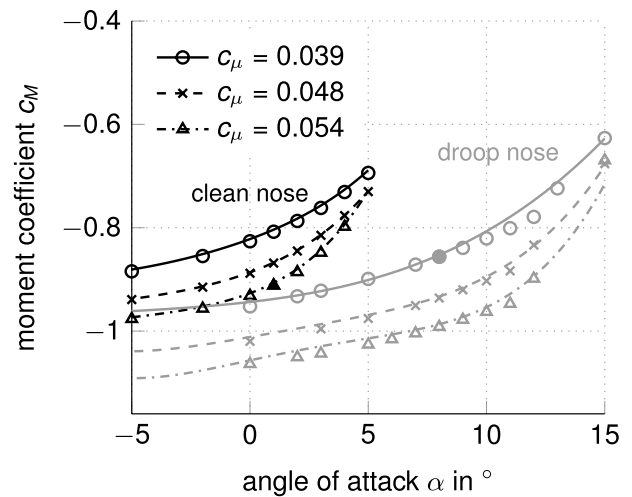


Fig. 6 Moment coefficient for clean nose and droop nose with $\delta_{n_i} = 65^\circ$

The moment coefficients (Fig. 6) are shifted to higher angles of attack as well. The results for comparable lift coefficients show a decreasing moment coefficient for the droop nose configuration (s. filled marks Fig. 6).

The steady derivatives $c_{L\alpha}$ and $c_{M\alpha}$ are directly known from the steady-state simulations. The mathematical smoothing functions for the clean nose configuration are given in [20]. The smoothing functions for the droop nose configuration result from Eqs. (12) and (13) to

$$\begin{aligned} c_{L\alpha,droop} = & (7.95 - 83.7 c_\mu) - (55.06 - 1265 c_\mu) \alpha \\ & - (0.954 - 22.74 c_\mu) 10^3 \alpha^2 \\ & + (0.48 - 13.48 c_\mu) 10^4 \alpha^3, \end{aligned} \tag{15}$$

$$\begin{aligned} c_{M\alpha,droop} = & -(0.39 - 17.7 c_\mu) + (13.02 - 251.6 c_\mu) \alpha \\ & + (1.92 - 44.7 c_\mu) 10^2 \alpha^2 \\ & - (10.56 - 275.6 c_\mu) 10^2 \alpha^3. \end{aligned} \tag{16}$$

The discrete results and corresponding smoothing functions are displayed in Figs. 7 and 8.

4.2 Unsteady aerodynamics

For the derivatives referring to heave \dot{h} and pitch $\dot{\alpha}$ motion, unsteady simulations are necessary.

The former approach of using harmonic pitching oscillations to determine the derivatives for rotational speed $\dot{\alpha}$ is described by Krukow and Dinkler [15]. A frequency of $f = 5.84$ Hz close to the first torsional frequency of the former structure was investigated with this approach [21].

Since eigenfrequencies vary with deviating properties and loads, it is useful to cover a range of frequencies. This can

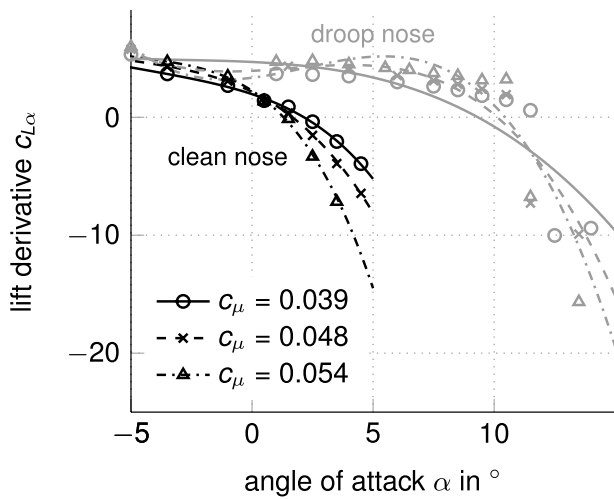


Fig. 7 Lift derivative $c_{L\alpha}$ for clean nose and droop nose with $\delta_{fl} = 65^\circ$

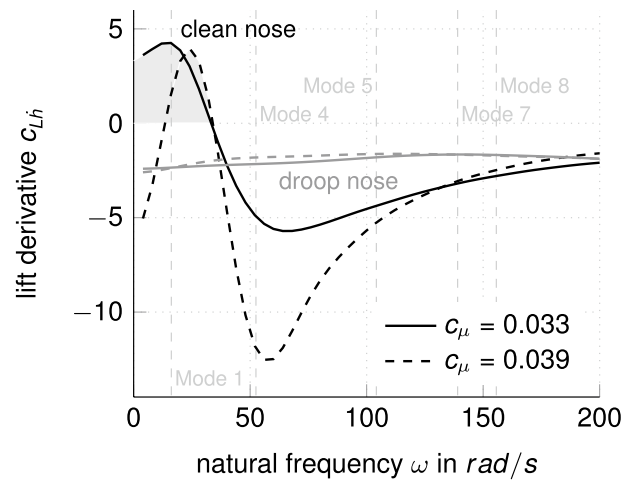


Fig. 9 Lift derivative c_{Lh} over natural frequency for clean nose and droop nose with $\alpha_T = 6^\circ$ and $\delta_{fl} = 65^\circ$

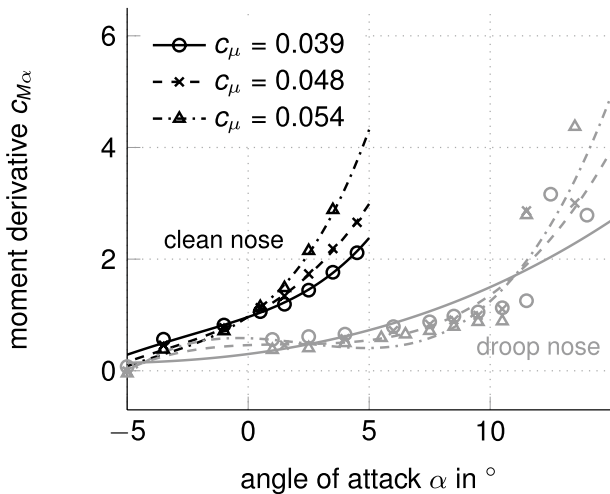


Fig. 8 Moment derivative $c_{M\alpha}$ for clean nose and droop nose with $\delta_{fl} = 65^\circ$

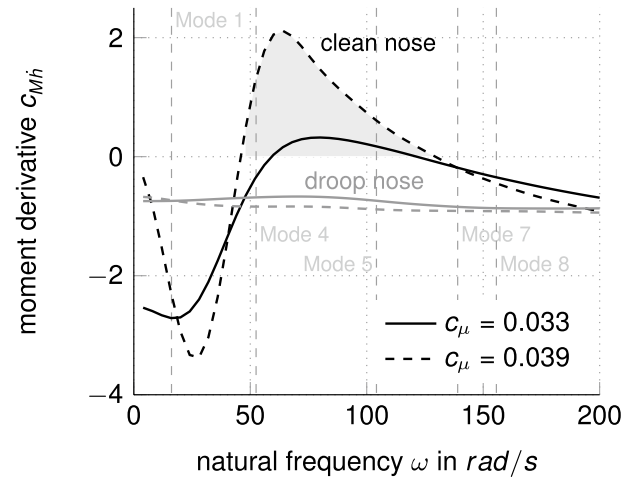


Fig. 10 Moment derivative c_{Mh} over natural frequency for clean nose and droop nose with $\alpha_T = 6^\circ$ and $\delta_{fl} = 65^\circ$

be achieved using an impulse motion [22, 23]. A Fourier transform is used to transform the system responses into the frequency domain. This results in a very high resolution of the entire frequency range.

The results of the lift and moment derivatives for heave (c_{Lh} , c_{Mh}) and pitch ($c_{L\dot{\alpha}}$, $c_{M\dot{\alpha}}$) over a range of natural frequencies ω at a trimm angle of attack α_T are shown in Figs. 9, 10, 11 and 12. The natural frequencies ω_i for the considered modes i of the wing with a full tank ($\eta_m = 1.3$) are marked by vertical lines. Different momentum coefficients c_μ are investigated. Positive derivatives indicate possible destabilisations and the corresponding areas are highlighted grey in the figures.

For the heave motion, a trimm angle of attack of $\alpha_T = 6^\circ$ is displayed (s. Figs. 9, 10). According to Fig. 5 the lift coefficient in this area has a negative gradient for the clean nose, also displayed in Fig. 7, which indicates instability. Figure 9 shows that this, however, only applies to natural frequencies up to 30 rad/s. Accordingly, only the first eigenmode is affected. The corresponding moment derivative c_{Mh} (Fig. 10) shows positive results for the clean nose configuration for natural frequencies ω from 45 to 130 rad/s. Therefore, here the modes 4 and 5 are concerned.

For the pitch motion at a trimm angle of attack of $\alpha_T = 0^\circ$, the clean nose shows positive values for the lift derivative $c_{L\dot{\alpha}}$ (Fig. 11) and negative values for the moment derivative $c_{M\dot{\alpha}}$ (Fig. 12) over the whole frequency range. The results of the droop nose with a momentum coefficient of $c_\mu = 0.033$

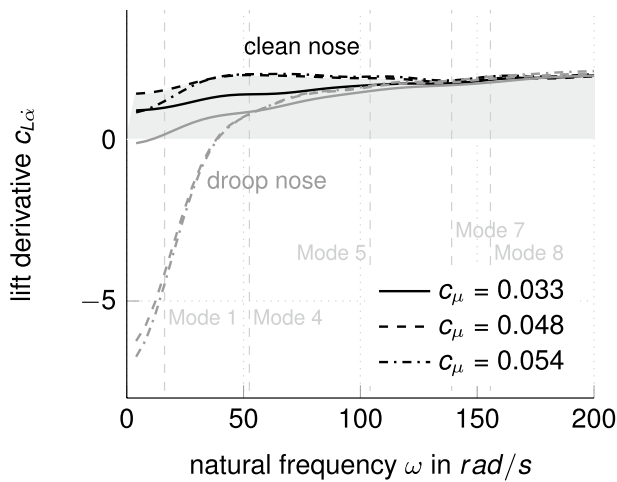


Fig. 11 Lift derivative $c_{L\dot{\alpha}}$ over natural frequency for clean nose and droop nose with $\alpha_T = 0^\circ$ and $\delta_{fl} = 65^\circ$

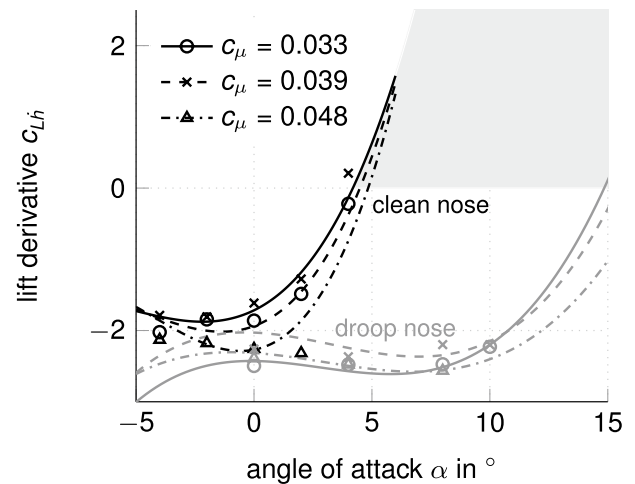


Fig. 13 Lift derivative c_{Lh} for clean nose and droop nose with $\omega = \omega_1$ and $\delta_{fl} = 65^\circ$

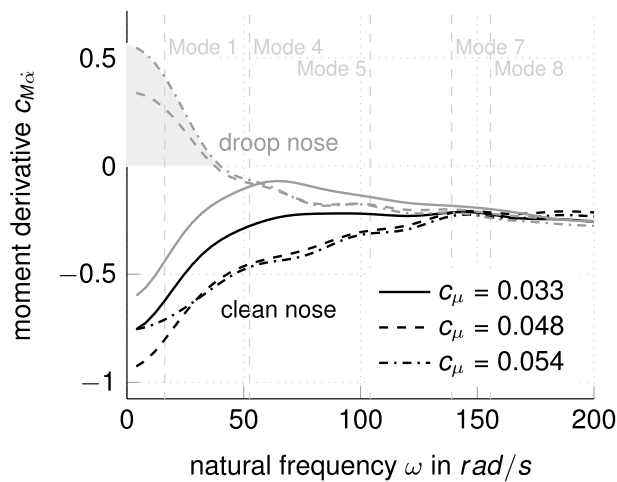


Fig. 12 Moment derivative $c_{M\dot{\alpha}}$ over natural frequency for clean nose and droop nose with $\alpha_T = 0^\circ$ and $\delta_{fl} = 65^\circ$

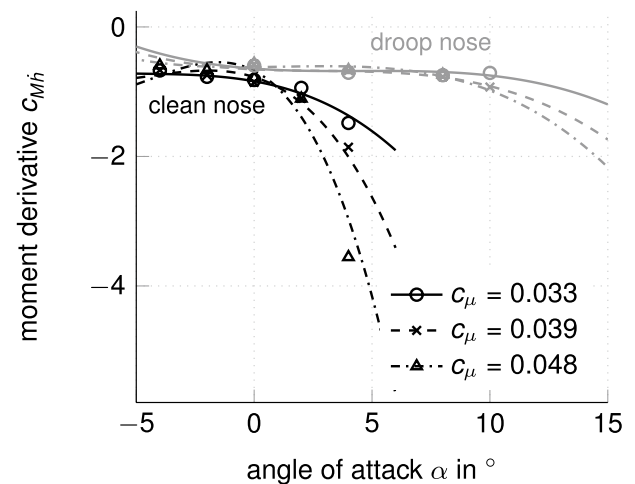


Fig. 14 Moment derivative c_{Mh} for clean nose and droop nose with $\omega = \omega_1$ and $\delta_{fl} = 65^\circ$

are comparable to the equivalent results of the clean nose. The results with greater momentum coefficients, however, indicate possible instabilities concerning the moment derivative $c_{M\dot{\alpha}}$ (Fig. 12) and stability for the lift derivative $c_{L\dot{\alpha}}$ (Fig. 11). These areas are limited to natural frequencies ω smaller than 40 rad/s. In the displayed case solely, the frequency of the first natural mode is located in the shaded area of the moment derivative $c_{M\dot{\alpha}}$.

For a better understanding of the behaviour depending on the angle of attack, Figs. 13, 14, 15 and 16 show the results over the angle of attack α for the frequency of the first natural mode ($\omega = \omega_1$). The results are again approximated by mathematical smoothing functions, based on the angle of attack α , the momentum coefficient c_{μ} and the natural frequency ω .

The lift derivative c_{Lh} displayed in Fig. 13 shows a sign change for both nose shapes comparable to Fig. 7. Angles of attack beyond $\alpha_{c_{Lh},max}$, therefore, lead to instabilities for the first natural frequency, whereas smaller angles of attack are stable. The moment derivative c_{Mh} displayed in Fig. 14 shows no sign change.

The lift derivative $c_{L\dot{\alpha}}$ displayed in Fig. 15 shows a sign change most notably for the clean nose configuration at high momentum coefficients c_{μ} and angles of attack greater than 0° . The moment derivative $c_{M\dot{\alpha}}$, however, indicates instabilities for high momentum coefficients c_{μ} and angles of attack smaller than 5° for the droop nose and, respectively, smaller than approximately -2° for the clean nose configuration.

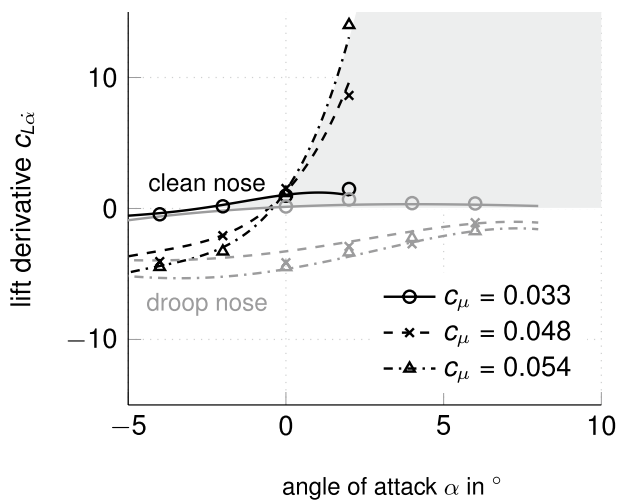


Fig. 15 Lift derivative $c_{L\dot{\alpha}}$ for clean nose and droop nose with $\omega = \omega_1$ and $\delta_{fl} = 65^\circ$

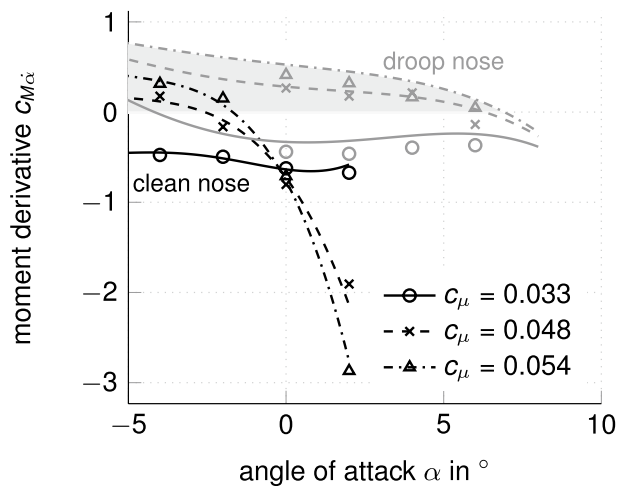


Fig. 16 Moment derivative $c_{M\dot{\alpha}}$ for clean nose and droop nose with $\omega = \omega_1$ and $\delta_{fl} = 65^\circ$

In summary, the investigations indicate instabilities in particular at low frequencies and angles of attack beyond the respective $\alpha_{c_{L,\max}}$.

5 Aeroelastic coupling

The strip theory delivers the aerodynamic loads

$$L = L_0 + A_0 x_A + A_1 \dot{x}_A, \tag{17}$$

at each strip, with a constant load vector L_0 , the aerodynamic stiffness A_0 and aerodynamic damping A_1 matrix. Equation (14) shows the involved degrees of freedom, vertical displacement h and torsional rotation α , which differ from the discretization of the finite element model. Thus, the

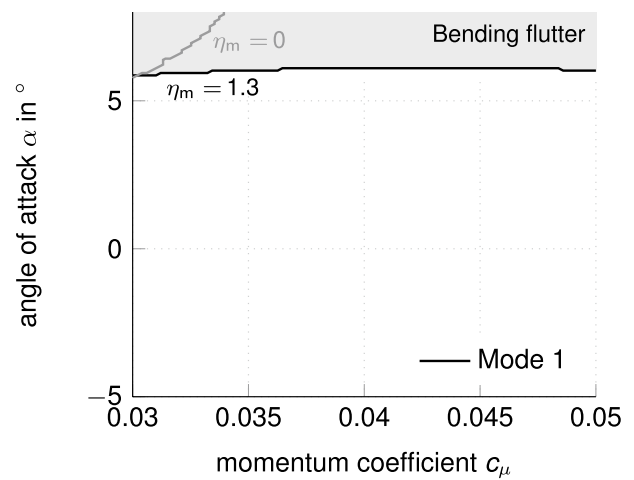


Fig. 17 Stability boundaries for clean nose with varying mass distribution with $\omega = \omega_1$

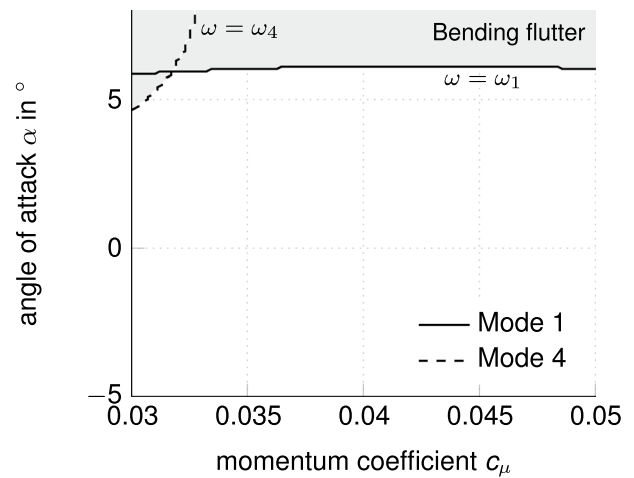


Fig. 18 Stability boundaries for clean nose with varying excitation frequency with $\eta_m = 1.3$

structural modes \hat{x}_i are transformed to be described solely by vertical displacement h and torsional rotation α . With the transformed modes \hat{x}_{Ai} , the modal approach in Eq. (3) accordingly leads to

$$\ddot{q}_i + \omega_i^2 q_i = \gamma_i g + \hat{x}_{Ai}^T L(q, \dot{q}). \tag{18}$$

Due to the additional loads on the right handside, the natural frequencies and natural modes of the system alter. The ROM stays based on the initial natural modes displayed in Fig. 3. The natural frequencies, however, are updated and the loads are calculated correspondingly to the adapted chosen frequency and calculated deformations.

The stability boundaries for different configurations are compared in Figs. 17, 18 and 19. Here, a range of angles of

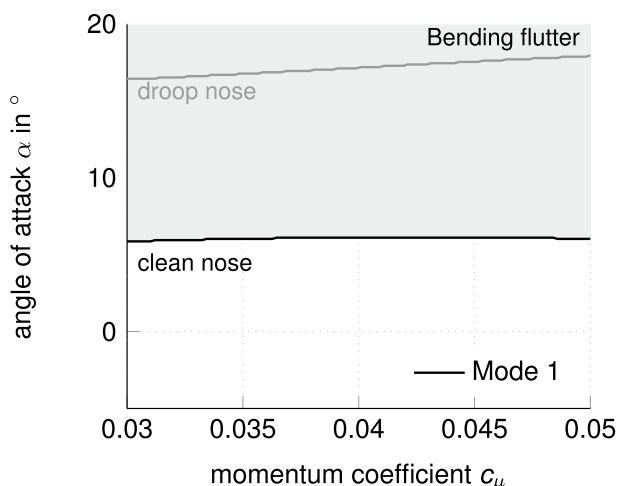


Fig. 19 Stability boundaries for clean nose and droop nose with $\omega = \omega_1$ and $\eta_m = 1.3$

attack, measured on the y -axis, and momentum coefficients, measured on the x -axis, is evaluated. All other parameters remain constant for the respective stability map. For each examined condition, it is checked whether a damped or undamped state is present. The transition from a damped to an undamped state is marked by a line, hereinafter referred to as the stability boundary. Critical areas are highlighted in grey. The basic flutter phenomenon is explained in detail in [20].

Figure 17 shows the stability boundaries for the clean nose configuration with different mass distributions ($\eta_m = 0$ and $\eta_m = 1.3$) and an exciting frequency equivalent to the first natural frequency ($\omega = \omega_1$). As pictured in Fig. 4, the first natural frequency of the lighter structure is slightly higher than the first natural frequency of the heavier structure. This is taken into account in the respective investigation.

The observable stability boundary for the heavy configuration results from the lift derivatives c_{Lh} shown in Fig. 13, corresponding to the sign change of the derivative c_{Lh} . A coupling of different modes is not observed, thus a pure first bending mode is present.

However, the interaction of the lighter structure and aerodynamic forces leads to coupling of the first three bending modes and, therefore, a higher first natural frequency. As pictured in Fig. 9, the derivative c_{Lh} indicates a more stable state with increasing frequencies. Therefore, the corresponding unstable area is significantly smaller.

Figure 18 shows the stability boundaries for the clean nose configuration at a full tank level ($\eta_m = 1.3$) at two different excitation frequencies ($\omega = \omega_1$ and $\omega = \omega_4$). Hence, different modes are addressed.

The resulting stability map for mode 1, addressed by $\omega = \omega_1$, equals the map displayed in Fig. 17 for $\eta_m = 1.3$.

Mode 4, addressed by $\omega = \omega_4$, enters no coupling and remains a clean second bending mode. The corresponding area, therefore, indicates bending flutter. Again, with increasing frequencies the lift derivative c_{Lh} in Fig. 9 indicates more stability. Therefore, the displayed stability boundary for the second bending mode is rather comparable to the stability boundary of the light structure ($\eta_m = 0$) in Fig. 17.

The largest differences can be seen in Fig. 19. Here, clean nose and droop nose with a full tank level ($\eta_m = 1.3$) and an excitation frequency equal to the respective first natural frequency ($\omega = \omega_1$) are compared.

For the droop nose, the stability boundary can be traced back to the lift derivatives c_{Lh} , displayed in Fig. 13. Since the maximum lift is shifted to higher angles of attack (s. Fig. 5), the change of sign of the lift derivative $c_{L\alpha}$ is shifted to the respective angles of attack (s. Fig. 7). Accordingly, the lift derivative c_{Lh} for the first natural frequency (s. Fig. 13) shows a change of sign at comparatively high angles of attack.

In comparison with the clean nose, the stability boundary of the droop nose configuration is shifted to higher angles of attack. However, there is no coupling of modes in case of the droop nose either. A pure first bending mode is observed here as well. The bending flutter phenomenon is driven by the pressure distribution shown in Fig. 2 and the resultant lift derivatives c_{Lh} .

6 Conclusion and future work

The paper outlines the investigation of aeroelastic effects of a circulation-controlled wing. A ROM, based on a full-scale three-dimensional finite element wing model, is extended by a parameterisation of essential properties. Since the natural frequencies and eigenvectors depend on the mass and stiffness distribution, the parameters η_m and η_k are introduced.

Steady and unsteady aerodynamics are based on two-dimensional flow simulations. An impulse method is used to determine the frequency dependency of the derivatives due to heave and pitch motion. Therefore, the ROM includes the natural frequency ω as a parameter. The forces are mapped onto the wing structure by strip theory.

Two profiles, clean and droop nose, are examined. Comparing the two profiles shows an increased angle of attack of maximum lift coefficient $\alpha_{c_{l,max}}$ by 10° for the droop nose. The needed blowing power for comparable lift coefficients is reduced significantly by including the droop nose.

Results of the frequency-dependent derivatives c_{Lh} and c_{Mh} show comparable values for the clean and droop nose depending on the shifted $\alpha_{c_{l,max}}$. In particular, the results of the moment derivative c_{Ma} indicate increasing areas of possible instabilities for the droop nose.

Aeroelastic coupling yields an additional flutter phenomenon due to circulation control. Bending flutter occurs corresponding to the maximum lift at low frequencies. Since $\alpha_{c_l, \max}$ is increased with the droop nose, the bending flutter is also shifted to higher angles of attack. It is shown, that varying the mass distribution affects the flutter boundary through changing frequencies. Differing the excitation frequency basically addresses different modes. Here, the second bending mode is addressed, which also shows pure bending flutter.

As aircrafts usually fly beneath well below $\alpha_{c_l, \max}$, the bending flutter is not likely to occur. Further studies on the impact of diverging properties of the wing structure are necessary to evaluate possible instabilities due to the moment derivative $c_{M\dot{\alpha}}$.

Acknowledgements Financial support has been provided by the German Research Foundation (Deutsche Forschungsgemeinschaft, DFG) in the framework of the Coordinated Research Centre SFB 880.

References

- Radespiel, R., Heinze, W.: SFB 880: fundamentals of high lift for future commercial aircraft. *CEAS Aeronaut. J.* **5**(3), 239–251 (2014)
- Flightpath, A.C.A.R.E.: 2050-Europes Vision for Aviation. Advisory Council for Aeronautics Research in Europe (2011)
- Burnazzi, M., Radespiel, R.: Design of a droopnose configuration for a Coanda active flap application. 51st AIAA Aerospace Sciences Meeting including the New Horizons Forum and Aerospace Exposition (2013)
- Lighthill, M.: Notes on the Deflection of Jets by Insertion of Curved Surfaces, and on the Design of Bends in Wind Tunnels. Aeronautics Research Council Reports and memoranda No. 2105 (1945)
- Korbacher, G.K.: Aerodynamics of powered high-lift systems. *Annu. Rev. Fluid Mech.* **6**(1), 319–358 (1974)
- Englar, R.J., Huson, G.: Development of advanced circulation control wing high-lift airfoils. *J. Aircr.* **21**(7), 476–483 (1984)
- Wood, N.: Circulation control airfoils past, present, future. Technical Report 85-0204, AIAA (1985)
- Pfingsten, K.C., Radespiel, R.: Experimental and numerical investigation of a circulation control airfoil. AIAA Paper 2009-533 (2009)
- Wilkerson, J.B.: Aeroelastic characteristics of a circulation control wing. Technical Report 76-0115, David W. Taylor Naval Ship Research and Development Center (1976)
- Haas, D.J., Chopra, I.: Static aeroelastic characteristics of circulation control wings. *J. Aircr.* **25**(10), 948–954 (1988)
- Haas, D.J., Chopra, I.: Flutter of circulation control wings. *J. Aircr.* **26**(4), 373–381 (1989)
- Young, T.: Outlines of experiments and inquiries respecting sound and light. *Philos. Trans. R. Soc. Lond.* **90**, 106–150 (1800)
- Englar, R.J., Smith, M., Kelley, S.M., Rover, R.C.: Application of circulation control to advanced subsonic transport aircraft, Part I—airfoil development. *J. Aircr.* **31**(5), 1160–1168 (1994)
- Englar, R.J., Smith, M., Kelley, S.M., Rover, R.C.: Application of circulation control to advanced subsonic transport aircraft, Part II—transport application. *J. Aircr.* **31**(5), 1169–1177 (1994)
- Krukow, I., Dinkler, D.: A reduced-order model for the investigation of the aeroelasticity of circulation-controlled wings. *CEAS Aeronaut. J.* **5**(2), 145–156 (2014)
- Sommerwerk, K., Haupt, M.C., Horst, P.: Aeroelastic performance assessment of a wing with Coandă effect circulation control via fluid-structure interaction. 31st AIAA Applied Aerodynamics Conference, San Diego (CA) (2013) AIAA 2013-2791
- Sommerwerk, K., Michels, B., Haupt, M.C., Horst, P.: Influence of engine modeling on structural sizing and approach aerodynamics of a circulation controlled wing. *CEAS Aeronaut. J.* **9**(1), 219–233 (2018)
- Schwamborn, D., Gardner, A.D., von Geyr, H., Krumbein, A., Lüdecke, H.: Development of the DLR TAU-Code for Aerospace Applications. 50th NAL International Conference on Aerospace Science and Technology, Bangalore (India) (2008)
- Spalart, P.R., Allmaras, S.R.: A one-equation turbulence model for aerodynamic flows. AIAA Paper 92-0439 (1992)
- Dinkler, D., Krukow, I.: Flutter of circulation-controlled wings. *CEAS Aeronaut. J.* **6**(4), 589–598 (2015)
- Sommerwerk, K., Krukow, I., Haupt, M.C., Dinkler, D.: Investigation of aeroelastic effects of a circulation controlled wing. *J. Aircr.* **53**(6), 1746–1756 (2016)
- Marques, A.N., Simões, C.F.C., Azevedo, J.L.F.: Unsteady aerodynamic forces for aeroelastic analysis of two-dimensional lifting surfaces. *J. Braz. Soc. Mech. Sci. Eng.* **28**(4), 474–484 (2006)
- Lisandrin, P., Carpentieri, G., Van Tooren, M.: An investigation over cfd-based models for the identification of nonlinear unsteady aerodynamics responses. *AIAA J.* **44**(9), 2043–2050 (2006)